

Tunable terahertz slow-light device based on triple plasmon-induced transparency on a patterned graphene metasurface

Bo-Yun Wang(王波云), Yao-Yang Dai(代耀阳), De-Bing Long(龙德兵), and Hua-Qing Yu(余华清)
Citation: Chin. Phys. B, 2026, 35 (**8**): 084211. DOI: 10.1088/1674-1056/ae86db
http://cpb.iphy.ac.cn; http://iopscience.iop.org/cpb

What follows is a list of articles you may be interested in

Dynamic control of topological phase of Dirac semimetallic terahertz metasurface

Chenglong Wang(王成龙), Zhihua Han(韩志华), Xiang Hou(侯翔), Yansheng Shao(邵延胜), Fangze Deng(邓方泽), Keke Cheng(程可可), Yuchao Li(李玉超), Ke Ma(马克), Yumeng Ma(马宇萌), Huiyun Zhang(张会云), Meng Liu(刘蒙), and Yuping Zhang(张玉萍)
Chin. Phys. B, 2026, 35 (**3**): 034207. DOI: 10.1088/1674-1056/adfbd8

Transmission property of one-dimensional Dirac-semimetal-defected photonic crystal in terahertz multi-bandgap

Ji-Kai Wang(王济凯), Li Jiang(姜丽), Xue-Fei Yang(杨雪菲), and Ji-He Zhao(赵继和)
Chin. Phys. B, 2026, 35 (**1**): 014209. DOI: 10.1088/1674-1056/ade4b3

Dynamically tunable multiband plasmon-induced transparency effect based on graphene nanoribbon waveguide coupled with rectangle cavities system

Zi-Hao Zhu(朱子豪), Bo-Yun Wang(王波云), Xiang Yan(闫香), Yang Liu(刘洋), Qing-Dong Zeng(曾庆栋), Tao Wang(王涛), and Hua-Qing Yu(余华清)
Chin. Phys. B, 2022, 31 (**8**): 084210. DOI: 10.1088/1674-1056/ac7e39

An ultrafast and low-power slow light tuning mechanism for compact aperture-coupled disk resonators

Bo-Yun Wang(王波云), Yue-Hong Zhu(朱月红), Jing Zhang(张静), Qing-Dong Zeng(曾庆栋), Jun Du(杜君), Tao Wang(王涛), Hua-Qing Yu(余华清)
Chin. Phys. B, 2020, 29 (**8**): 084211. DOI: 10.1088/1674-1056/ab9df1

Tunable plasmon-induced transparency based on asymmetric H-shaped graphene metamaterials

Yu-Chen Tian(田雨宸), Wei Jia(贾微), Pei-Wen Ren(任佩雯), Chun-Zhen Fan(范春珍)
Chin. Phys. B, 2018, 27 (**12**): 124205. DOI: 10.1088/1674-1056/27/12/124205

Tunable terahertz slow-light device based on triple plasmon-induced transparency on a patterned graphene metasurface

Bo-Yun Wang(王波云)[1,2,†], Yao-Yang Dai(代耀阳)[1], De-Bing Long(龙德兵)[1], and Hua-Qing Yu(余华清)[1]

[1] *School of Physics and Electronic-Information Engineering, Hubei Engineering University, Xiaogan* 432000, *China*
[2] *Wuhan National Laboratory for Optoelectronics, Huazhong University of Science and Technology, Wuhan* 430074, *China*

(Received 21 May 2026; revised manuscript received 25 June 2026; accepted manuscript online 7 July 2026)

The present study proposes a reconfigurable metasurface comprising four graphene rectangles together with five graphene strips, designed to achieve triple plasmon-induced transparency (PIT). The coupled mode theory-based theoretical analysis demonstrates a high level of agreement with finite-difference time-domain simulation results. This graphene-based triple-PIT device enables dynamic tuning of its Fermi level and carrier mobility. For the prepared triple-PIT system, the group index varies from 1134 to 2020 with increasing graphene Fermi level in the range of 0.8–1.2 eV. Conversely, the group index ranges from 1123 to 2079 with increasing graphene carrier mobility in the range of 2.5–4.5 $m^2/(V{\cdot}s)$. Additionally, the maximum group index (2079) of this device is achieved at the 1.0 eV Fermi level and the 4.5 $m^2/(V{\cdot}s)$ carrier mobility, which markedly exceeds that of conventional terahertz slow-light structures. Furthermore, the device exhibits good tolerance to design and fabrication deviations. It thus provides useful design guidance for high-performance terahertz slow-light devices.

Keywords: plasmon-induced transparency (PIT), slow-light device, terahertz, patterned graphene metasurface

PACS: 42.25.Bs, 81.05.ue, 47.11.Bc

DOI: 10.1088/1674-1056/ae86db **CSTR:** 32038.14.CPB.ae86db

1. Introduction

Metasurfaces, artificially engineered composite structures,[1] have transformed wave manipulation by enabling extraordinary optical properties, such as negative refraction,[2] electromagnetic cloaking,[3] and perfect lensing. However, the functionality of conventional metal-based metasurfaces is generally fixed after fabrication, as their optical responses are largely insensitive to external stimuli.[4,5] This inherent limitation restricts their application in reconfigurable optical devices, intelligent sensing, and next-generation adaptive optoelectronic systems.[6,7] To address this issue, considerable research efforts have focused on material systems with active tuning capabilities. Among the various candidates, graphene has attracted significant attention due to its exceptional potential.[8]

Graphene, a 2D hexagonal honeycomb lattice material, consists of sp^2-hybridized carbon atoms, and its remarkable optical properties have been extensively studied.[9–11] Importantly, graphene can interact with incident electromagnetic fields to excite surface plasmon polaritons (SPPs),[12] which are electromagnetic modes formed at graphene interfaces, originating from the collective oscillations of surface electrons, thereby providing a microphysical basis for wave manipulation in metasurfaces.[13] Meanwhile, SPPs induce strong local field enhancement, which can facilitate bright–dark mode coupling and thus lead to the electromagnetically induced transparency (EIT) effect.

EIT, a coherent optical phenomenon, arises from quantum interference effects.[14] It originates from electromagnetic field–energy level interactions within a broad absorption band, resulting in an extremely narrow transmission window and a pronounced phase shift at high frequencies. Slow-light effects and their associated applications are directly enabled by this phenomenon. Similarly, plasmon-induced transparency (PIT) shows strong similarity to EIT,[14–17] as it is associated with destructive interference generated by the resonance of bright and dark modes. This mechanism underlies the triple-PIT slow-light functionality of the prepared graphene metasurface.[18–20] Recently, substantial progress has been made in graphene metasurface-based slow-light devices. Notably, Xu *et al.* employed a graphene structure distributed in two layers, which requires precise control of the relative alignment and thickness of the two graphene layers, thereby increasing design and fabrication complexity.[21] In contrast, the present work adopts a monolayer patterned graphene structure, achieving an enhanced triple-PIT effect through an optimized geometric configuration, which simplifies the design and fabrication process while maintaining high performance.

In this work, a metasurface array is designed to achieve dynamically tunable triple-PIT. This metasurface consists of four graphene rectangles and five graphene strips. To investigate the physical mechanisms associated with the triple-PIT effect, the *n*th-order coupled mode theory (CMT) is used.

[†]Corresponding author. E-mail: wangboyun@alumni.hust.edu.cn

© 2026 Chinese Physical Society and IOP Publishing Ltd. All rights, including for text and data mining, AI training, and similar technologies, are reserved.

The obtained calculations show strong agreement with finite-difference time-domain (FDTD)-based numerical simulations, particularly for the triple-PIT system where n is 4. By precisely modulating the Fermi level and carrier mobility of graphene, the prepared triple-PIT system exhibits a group index ranging from 1134 to 2020 (the corresponding group delay varies from 0.57 ps to 1.01 ps) with increasing Fermi level from 0.8 eV to 1.2 eV. Conversely, the group index varies from 1123 to 2079 (the corresponding group delay varies from 0.56 ps to 1.04 ps) with increasing carrier mobility from 2.5 $m^2/(V{\cdot}s)$ to 4.5 $m^2/(V{\cdot}s)$. The maximum group index is as high as 2079 (the corresponding group delay is 1.04 ps) at $\mu = 4.5$ $m^2/(V{\cdot}s)$ and $E_F = 1.0$ eV, which shows that the slow-light performance is much better than that of previous slow-light devices. Because of the continuity and simplicity of our structures, the triple-PIT effect can be dynamically tuned by changing the graphene Fermi level and carrier mobility rather than changing the geometry. Moreover, the proposed structure shows good tolerance to fabrication deviations. Under typical geometric parameter variations, such as parameter H_3 varying by 0.1 μm or parameter L_5 by 0.2 μm, the group index exhibits only minor deviations from its optimal value. These findings highlight the potential of the device for reliable practical applications. Therefore, the results of this study provide a theoretical foundation for the design and fabrication of slow-light devices, optical switches and modulators.

2. Structure and theoretical analysis

2.1. Structural model

In this work, MATLAB (version R2025a) and Lumerical FDTD Solutions (version 2020R2) are used to quantitatively assess the slow-light properties and field distributions associated with the PIT phenomenon. In this simulation, a transverse-magnetic-polarized linear plane wave propagating along the negative z-axis serves as the excitation source.[22,23] Periodic boundary conditions are applied along the x- and y-directions, while perfectly matched layer absorbing boundary conditions are set for the z-direction. Meanwhile, the spatial mesh size is defined as $\Delta x = \Delta y = \Delta z = 0.05$ μm.[24,25] Moreover, the temperature and simulation time are 300 K and 10000 fs, respectively. Given that incident light propagates through air, the ambient refractive index is assumed to be 1.

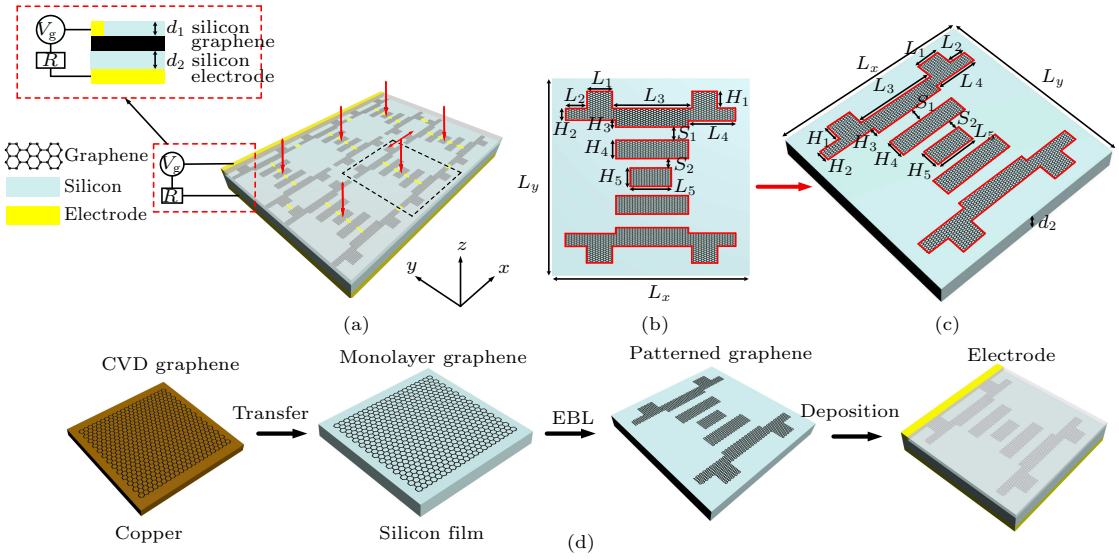


Fig. 1. (a) 3D schematic diagram showing the prepared graphene metasurface. (b) 2D top view and (c) side view of the structural unit. (d) Schematic diagram showing the fabrication process of the proposed metasurface structure.

As illustrated in Fig. 1(a), dielectric silicon (thicknesses, $d_1 = 0.05$ μm, $d_2 = 0.15$ μm) is utilized as the substrate for the upper and lower layers. Monolayer graphene is embedded within the Si layer, and its relative permittivity is 11.7 (Palik). The refractive index of Si is 3.42. With respect to graphene, its Fermi level and carrier mobility are controlled by two metallic electrodes, which act together with the Si substrate as a capacitor. A bias voltage is applied to dynamically regulate these properties. Consequently, the Fermi level can be tuned within 0.8–1.2 eV, and the carrier mobility ranges from 2.5 $m^2/(V{\cdot}s)$ to 4.5 $m^2/(V{\cdot}s)$. Figure 1(b) presents a schematic illustration of the geometric parameters of the unit cell. $L_x = L_y = 6$ μm, $L_1 = 0.6$ μm, $L_2 = H_1 = 0.5$ μm, $L_3 = 2.6$ μm, $L_4 = 1.1$ μm, $L_5 = 1.4$ μm, $H_2 = 0.4$ μm, $H_3 = 0.2$ μm, $H_4 = 0.6$ μm, $H_5 = 0.6$ μm, $S_1 = 0.3$ μm, $S_2 = 0.2$ μm. Figure 1(c) shows the side view of the structural unit, where the dielectric Si substrate is covered by single-layer graphene sheets.

Figure 1(d) shows the possible fabrication process of the designed patterned graphene metasurface. It offers crucial insights into its assembly. First of all, graphene is grown on a copper foil through chemical vapor deposition (CVD) at a temperature of 1050 °C.[26,27] Secondly, the graphene layer

is meticulously transferred onto a silicon substrate, followed by acetone rinsing to dissolve the residual photoresist.[28] Thirdly, the graphene is patterned using electron beam lithography (EBL).[28] Lastly, metal is deposited onto the patterned graphene, and a metal electrode is deposited at the bottom of the silicon substrate. A silicon layer measuring 50 nm in thickness is precisely deposited atop the patterned graphene. When x-polarized light vertically irradiates the entire structure, the triple-PIT effects are observed.

Three transparent windows emerge near the three dips of the Lorentz curves. This is a triple-PIT phenomenon,[29] as shown by the blue solid line in Fig. 2(a). When the incident light interacts with the structure, G2, a single graphene strip, together with G3 and G4, each consisting of two separate strips, generate a Lorentzian resonance, and serve as bright modes. G1, which consists of four separate graphene rectangles, functions as a dark mode. Although incident light cannot directly excite the dark mode, the latter interacts with the local field arising from the coupling of incident light with bright modes. The dark mode interferes destructively with each of the three bright modes corresponding to G2, G3, and G4, producing three transmission peaks located at f_{p3}, f_{p1}, and f_{p2}, thus leading to a significant triple-PIT phenomenon in the terahertz range. Since the incident plane wave is relatively weak, nonlinear effects of graphene are neglected in this analysis.[30]

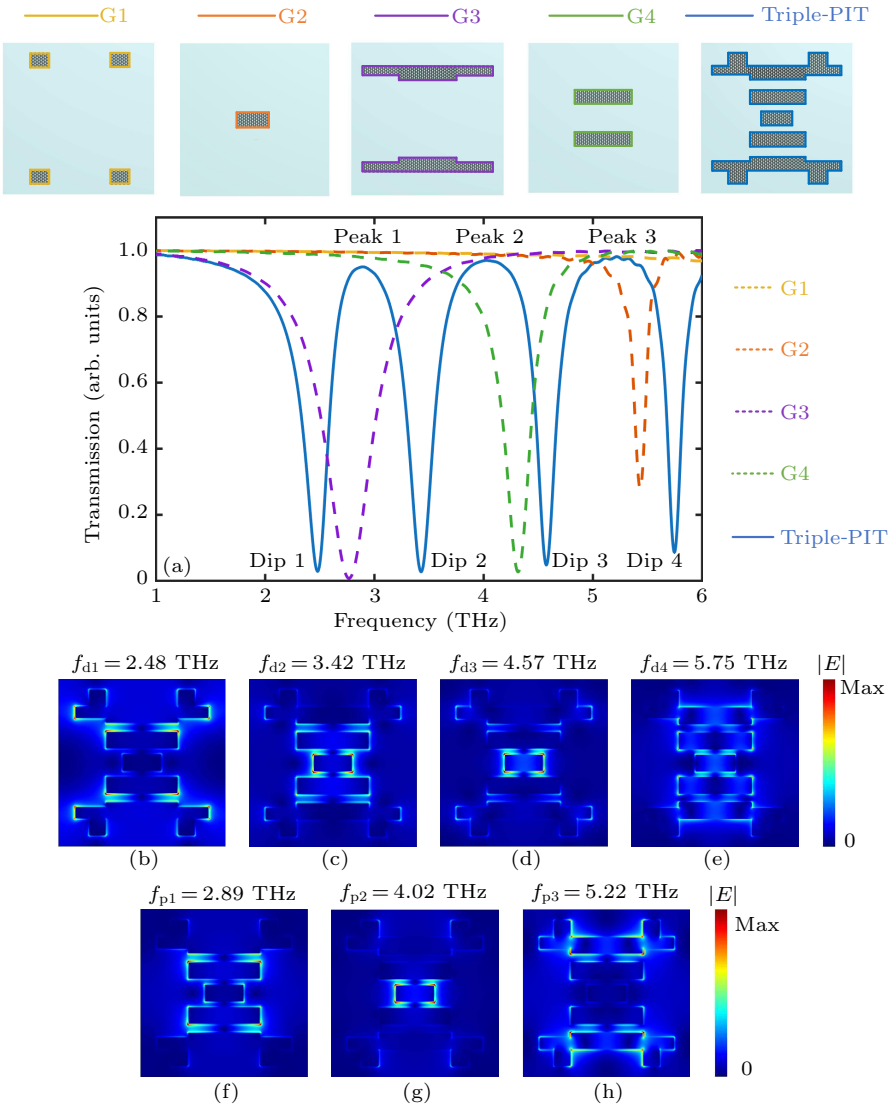


Fig. 2. (a) Transmission spectra for each partial graphene structure with $E_F = 1.0$ eV and $\mu = 3.5$ m^2/(V·s). (b)–(e) Normalized electric field distributions at four transmission dips in the proposed graphene metasurface structure. (f)–(h) Normalized electric field distributions at three transmission peaks of the proposed graphene metasurface structure.

To further investigate the physical mechanisms of the triple-PIT effect in the proposed graphene metasurface, normalized electric field distributions at four transmission dips and three peaks are analyzed. From Figs. 2(b)–2(e), the electric field energy at dip 1 is distributed along the left and right edges of G3 and within the region between G3 and G4. The field distributions at dip 2 and dip 3 are relatively similar, both appearing at the four corners of G2, although the field at dip 3 is more concentrated at these corners. At dip 4, a uniform distribution of electric field energy is observed across the en-

tire structure. Figures 2(f)–2(h) present the normalized electric field distributions at each transmission peak. For peak 1, the electric field energy is mainly concentrated between G3 and G4. Similar to dip 3, the electric field at peak 2 is primarily concentrated at the four corners of G2. At peak 3, the electric field energy is predominantly localized at the interface between G4 and G3, as well as along the lower edge of G3.

2.2. Theoretical analysis

In FDTD simulations, a nominal thickness of 1 nm is assigned to graphene, which is implemented through a transition boundary condition.[31] For monolayer graphene, its conductivity is primarily determined by intraband electron–photon scattering and interband photon-stimulated transitions, as described by the Kubo formula[32]

$$\sigma = \sigma^{\text{intra}} + \sigma^{\text{inter}}. \tag{1}$$

The electrical conductivity of single-layer graphene arises from intraband electron scattering, with an additional contribution from photon-induced interband transitions. These components can be separately expressed using the following equations for intraband conductivity σ^{intra} and interband conductivity σ^{inter}:

$$\sigma^{\text{intra}} = \frac{e^2 E_{\text{F}}}{\pi\hbar^2(\omega + \mathrm{i}\tau^{-1})}\mathrm{i}, \tag{2}$$

$$\sigma^{\text{inter}} = \frac{e^2}{4\pi}\left[1 + \frac{\mathrm{i}}{\pi}\ln\frac{\hbar^2(\omega+\mathrm{i}\tau^{-1})^2 - 2E_{\text{F}}}{\hbar(\omega+\mathrm{i}\tau^{-1})^2 + 2E_{\text{F}}}\right], \tag{3}$$

where e denotes the elementary charge, E_{F} represents the Fermi energy, and $\hbar$ is the reduced Planck's constant; ω is the angular frequency, τ is the relaxation time, given by $\tau = \mu E_{\text{F}}/ev_{\text{F}}^2$, and i is the imaginary unit. At room temperature (300 K), when working in the terahertz band, the direct transitions of inter-band photons can be neglected due to the condition of $E_{\text{F}} > k_{\text{B}}T = 25.85$ meV. Therefore, the graphene conductivity (σ) can be effectively approximated by the Drude model[33]

$$\sigma \approx \sigma^{\text{intra}} = \frac{e^2 E_{\text{F}}}{\pi\hbar^2(\omega + \mathrm{i}\tau^{-1})}\mathrm{i}, \tag{4}$$

where μ denotes the carrier mobility of graphene, while v_{F} ($\approx 10^6$ m/s) represents the Fermi velocity. One graphene layer is positioned between two silicon layers in the proposed structure. Due to the symmetric distribution of the same dielectric material on both sides of graphene, its effective dielectric constant is nearly consistent with the actual dielectric constant. The propagation constant β in a homogeneous dielectric medium can be derived by combining Maxwell's equations with electromagnetic boundary conditions as follows:[34]

$$\beta = k_0\sqrt{\varepsilon_{\text{Si}} - \left(\frac{2\varepsilon_{\text{Si}}}{\eta_0\sigma}\right)^2}, \tag{5}$$

in which k_0 denotes the wavenumber in free space, η_0 represents the intrinsic impedance of free space, and ε_{Si} is the relative permittivity of Si. This relation clearly indicates that the propagation characteristics of SPPs, characterized by β, are jointly determined by both the bulk properties of the surrounding medium and the surface conductivity σ of this two-dimensional material. Additionally, the effective refractive index and intrinsic quality factor can be expressed as $n_{\text{eff}} = \beta/k_0$ and $Q_{\text{int}} = \text{Re}(n_{\text{eff}})/\text{Im}(n_{\text{eff}})$, respectively.

Significantly, CMT is employed to clarify the physical mechanisms associated with the $(n-1)$th-order PIT effect in the proposed planar monolayer graphene metasurface structure. Here, $(n-1)$ represents the PIT order, namely, the number of transparency windows. Figure 3 presents the CMT-simulated PIT effect. The equivalent modes are defined as S_1, S_2, …, S_{n-1}, and S_n in the nth-order excitation states. Waves propagating in the positive and negative directions are denoted by subscripts + and −, respectively. Furthermore, superscripts in and out are used to represent incoming and outgoing waves, respectively.

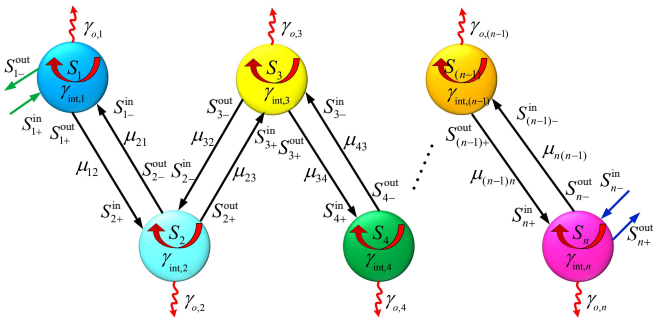


Fig. 3. Sketch map showing the CMT-modeled PIT effect.

With respect to the energy amplitude in the oscillatory radiation mode a_n, the transfer equation corresponding to the nth resonator can be expressed below:[35]

$$\begin{pmatrix} \gamma_1 & -\mathrm{i}\mu_{12} & \dots & -\mathrm{i}\mu_{1n} \\ -\mathrm{i}\mu_{21} & \gamma_2 & \dots & -\mathrm{i}\mu_{2n} \\ \vdots & \dots & \ddots & \vdots \\ -\mathrm{i}\mu_{n1} & -\mathrm{i}\mu_{n1} & \dots & \gamma_n \end{pmatrix} \begin{pmatrix} a_1 \\ a_2 \\ \vdots \\ a_n \end{pmatrix} = \begin{pmatrix} -\gamma_{o,1}^{1/2} & 0 & \dots & 0 \\ 0 & -\gamma_{o,2}^{1/2} & \dots & 0 \\ \vdots & \dots & \ddots & \vdots \\ 0 & 0 & \dots & -\gamma_{o,n}^{1/2} \end{pmatrix} \begin{pmatrix} S_{1+}^{\text{in}} + S_{1-}^{\text{in}} \\ S_{2+}^{\text{in}} + S_{2-}^{\text{in}} \\ \vdots \\ S_{n+}^{\text{in}} + S_{n-}^{\text{in}} \end{pmatrix}, \tag{6}$$

where $\gamma_n = \mathrm{i}\omega - \mathrm{i}\omega_n - \gamma_{\text{int},n} - \gamma_{o,n}$ and ω_n denotes the resonant angular frequency of the nth mode. For the nth mode, $\gamma_{\text{int},n} = \omega_n/(2Q_{\text{int},n})$ is the intrinsic loss coefficient, $\gamma_{o,n} = \omega_n/(2Q_{o,n})$ denotes the decay rate coefficient resulting from the escaping power within the external space, and μ_{mn} $(m \neq n)$ is the coupling coefficient between the mth mode and the nth mode. In this study, $\gamma_{\text{int},n} = \gamma_{o,n} = 10^{11}$ rad/s and $\mu_{mn} = 10^{11}$ rad/s, respectively. $Q_{\text{int},n}$ represents the intrinsic quality factor due to

the intrinsic loss of the nth mode, $Q_{o,n}$ represents the quality factor arising from the radiation loss of the nth mode, and $Q_{t,n}$ represents the total quality factor of the nth mode. These parameters satisfy the relation $1/Q_{t,n} = 1/Q_{int,n} + 1/Q_{o,n}$. $Q_{t,n} = f/\Delta f$, where f is the resonance frequency and Δf is the full width at half maximum (FWHM). Fitting total quality factors can be calculated by the transmission spectra of the simulation triple-PIT. In addition, $Q_{int,n}$ can be determined by $Q_{int,n} = \mathrm{Re}(n_{eff})/\mathrm{Im}(n_{eff})$. Therefore, $Q_{o,n}$ can be derived as $Q_{o,n} = Q_{int,n}Q_{t,n}/(Q_{int,n} - Q_{t,n})$.

For the nth resonator, the transmission coefficient can be expressed as follows:[35]

$$\begin{aligned} t_n = \frac{S_{n+}^{\mathrm{out}}}{S_{1+}^{\mathrm{in}}} &= \mathrm{e}^{\mathrm{i}(\varphi_1+\varphi_2\cdots+\varphi_{n-1})} - \gamma_{o,1}^{1/2}\xi_1\,\mathrm{e}^{\mathrm{i}(\varphi_1+\varphi_2\cdots+\varphi_{n-1})} \\ &\quad - \gamma_{o,2}^{1/2}\xi_2\,\mathrm{e}^{\mathrm{i}(\varphi_2+\varphi_3\cdots+\varphi_{n-1})} - \ldots \\ &\quad - \gamma_{o,(n-1)}^{1/2}\xi_{n-1}\,\mathrm{e}^{\mathrm{i}\varphi_{n-1}} - \gamma_{o,n}^{1/2}\xi_n, \end{aligned} \tag{7}$$

where $\xi_n = a_n/S_{1+}^{\mathrm{in}}$. φ_n denotes the phase difference between two adjacent modes and can be determined by $\varphi_n = \mathrm{Re}(\beta)d_n$. In the nth modes, the wavefront locations coincide with those of the incident wave, thus $\varphi_n = 0$.

For the PIT system, its theoretical transmittance can be expressed as follows:

$$T_n = |t_n|^2. \tag{8}$$

When $n = 4$, the system's transmission coefficient with triple-PIT can be determined as follows:

$$\begin{aligned} t_4 = \frac{S_{4+}^{\mathrm{out}}}{S_{1+}^{\mathrm{in}}} &= \mathrm{e}^{\mathrm{i}(\varphi_1+\varphi_2+\varphi_3)} - \gamma_{o,1}^{1/2}\xi_1\,\mathrm{e}^{\mathrm{i}(\varphi_1+\varphi_2+\varphi_3)} \\ &\quad - \gamma_{o,2}^{1/2}\xi_2\,\mathrm{e}^{\mathrm{i}(\varphi_2+\varphi_3)} - \gamma_{o,3}^{1/2}\xi_3\,\mathrm{e}^{\mathrm{i}\varphi_3} - \gamma_{o,4}^{1/2}\xi_4. \end{aligned} \tag{9}$$

3. Results and analysis

3.1. Simulations and analysis of triple-PIT effect through adjusting graphene's Fermi level

Graphene exhibits significant advantages in dynamic tunability.[36–38] This property enables modulation of the PIT effect by tuning the Fermi level or carrier mobility of graphene, without modifying the predefined geometric parameters of the structure. The relationship between the Fermi level of graphene and gate voltage can be[39,40]

$$E_{\mathrm{F}} = \hbar v_{\mathrm{F}}\sqrt{\frac{\pi\varepsilon_0\varepsilon_{\mathrm{d}}V_{\mathrm{g}}}{d_{\mathrm{sub}}e}}, \tag{10}$$

where V_{g} denotes the gate voltage, ε_0 represents the vacuum permittivity, ε_{d} indicates the relative permittivity of the dielectric Si layer, and d_{sub} denotes the inter-electrode distance. According to Eq. (25), the Fermi level of graphene can be dynamically tuned by controlling the gate voltage. As shown in Fig. 4, the Fermi level increases with increasing gate voltage, enabling dynamic modulation of the spectral response. Consequently, the PIT system can be tuned by modulating the Fermi level of graphene.

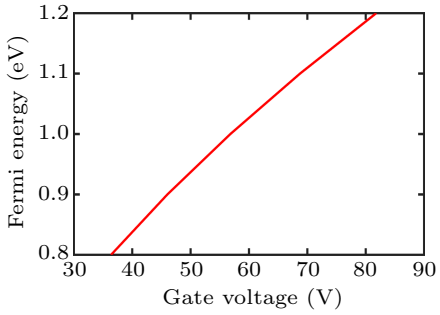


Fig. 4. Graphene's Fermi energies versus the applied gate voltage.

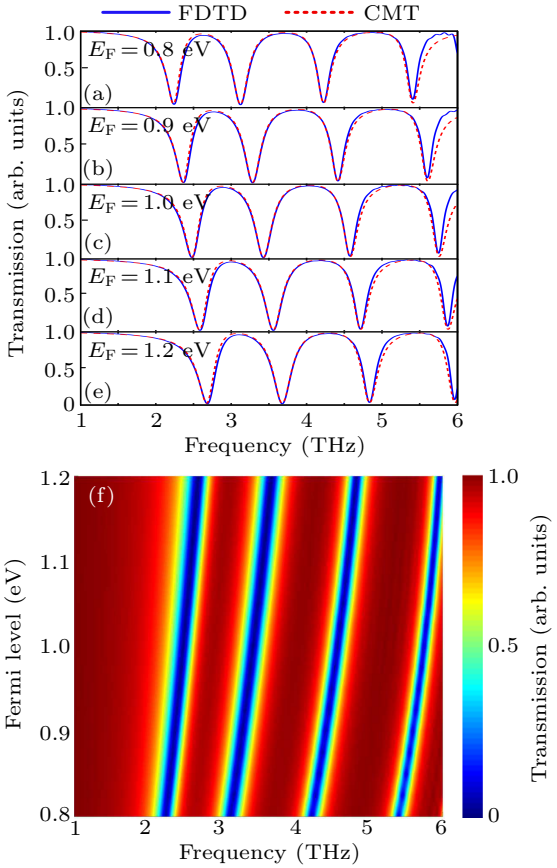


Fig. 5. (a)–(e) Simulated transmission spectra for coupled modes at Fermi levels of 0.8–1.2 eV and carrier mobility of $\mu = 3.5$ m^2/(V·s). (f) Evolution diagram for triple-PIT with different Fermi levels.

During the analysis, the carrier mobility of graphene was maintained at 3.5 m^2/(V·s), while the Fermi level was varied to investigate its influence on the transmission characteristics of the triple-PIT system. Based on FDTD simulations, the resonant frequencies within the transparency dips shift with increasing Fermi level. As illustrated in Figs. 5(a)–5(e), the tunability of the system is clearly verified by modulating the Fermi level, as evidenced by the independent control of the center frequencies of the triple-PIT transparency windows. The FDTD numerical simulations are consistent with the theoretical CMT fitting results, where the transmission curves obtained from FDTD (blue solid line) show good agreement with

those from CMT (red dashed line). In Fig. 5(f), the triple-PIT window exhibits a continuous blue shift toward higher frequencies in an approximately linear manner with increasing Fermi level, while the transmittance remains nearly unchanged. Furthermore, the evaluation of multi-PIT phenomena relies on a key criterion, whereby the emergence of a transparency window must coincide with the resonant frequency of a bright mode, facilitated by coupling with a dark mode. Consequently, other complex resonances of the graphene structure above 6 THz are excluded from this analysis,[30] as they do not satisfy this essential requirement.

Transmission profiles of the triple-PIT system under different Fermi level conditions are presented, illustrating the structural feature of dynamic tunability. A clear shift of the triple-PIT window toward higher frequencies is observed with increasing Fermi level. This shift arises because, for monolayer graphene, the SPP wave vector is given by $k_{\mathrm{SPPs}} = 2\pi^2\hbar f_{\mathrm{r}}^2/(\alpha_0 E_{\mathrm{F}} c)$ and $k_{\mathrm{SPPs}} \propto 1/W$, where f_{r} denotes the resonance frequency, W represents the length in the x-direction within one unit cell, and $\alpha_0 = e^2/\hbar$ denotes the fine structure constant. The resonance frequency can be expressed as $f_{\mathrm{r}} \propto \sqrt{\alpha_0 E_{\mathrm{F}} c/(2\pi^2\hbar W)}$.[41] The resonance frequency is directly proportional to the square root of the Fermi level. Consequently, the resonance frequency shifts to higher values, a phenomenon referred to as a blue shift.[42]

3.2. Simulations and analysis of triple-PIT effect through adjusting graphene's carrier mobility

To investigate the influence of carrier mobility on the prepared graphene structure, a systematic analysis of its effect on the optical response is also conducted using FDTD simulations. A series of simulations is performed with the Fermi level fixed at 1.0 eV. By incrementally varying the carrier mobility and analyzing the corresponding transmission spectra using the FDTD method, a consistent trend is observed, where the resonant frequencies associated with the dips of the triple-PIT windows gradually shift with increasing carrier mobility. This behavior indicates that variations in carrier mobility can effectively modify the coupling conditions within the structure, thereby altering the spectral positions of the PIT resonances. These findings emphasize the importance of carrier mobility as a key tuning parameter in graphene-based plasmonic systems. As illustrated in Fig. 6(a), different carrier mobilities correspond to distinct transmission spectra, and the triple-PIT system exhibits an increase in the maximum transmission peak as the carrier mobility increases, indicating that higher carrier mobility enhances transmission efficiency. Figure 6(b) presents an evolution diagram for triple-PIT transmission spectra under different graphene carrier mobilities, showing that the triple-PIT window continuously redshifts toward lower frequencies in an approximately linear manner as the carrier mobility increases.

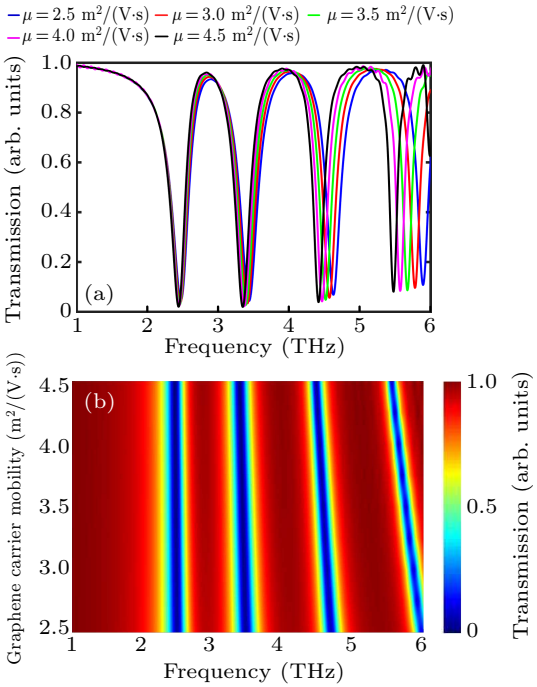


Fig. 6. (a) Effect of graphene carrier mobility on plasmon-induced transparency at carrier mobilities of 2.5–4.5 m^2/(V·s) (E_{F} = 1.0 eV). (b) Evolution diagram for triple-PIT with different carrier mobilities.

The most critical observation is the red shift with increasing carrier mobility. As indicated by the relation $\mu = \tau e v_{\mathrm{F}}^2/E_{\mathrm{F}}$, carrier mobility is negatively correlated with the Fermi level of graphene. As a result, the resonance frequency is given by $f_{\mathrm{r}} \propto \sqrt{\alpha_0 c e \tau v_{\mathrm{F}}^2/(2\pi^2\hbar\mu W)}$. Hence, an increase in carrier mobility induces a red shift in the resonance curve. In addition, similar red shifts can be achieved through graphene doping, enhanced surface conductivity, and increased electronic activity within graphene. Thus, dynamic tuning of the triple-PIT system can be realized by adjusting the carrier mobility of graphene.

3.3. Performance analysis of slow-light devices

The PIT effect exhibits significant potential for optical data storage applications. By substantially reducing the group velocity of light, it enables prolonged interaction between light and the storage medium. This extended interaction time facilitates effective writing and retention of optical information. The phase shift in the PIT effect is defined as $\theta(\omega) = \arg(t_n)$. The group delay can be expressed as $\tau_{\mathrm{g}} = \partial\theta(\omega)/\partial\omega$. A key parameter governing slow-light performance is the group index n_{g}, which is directly derived from the steep dispersion associated with high-quality-factor resonance peaks and is expressed as[43]

$$n_{\mathrm{g}} = \frac{c}{v_{\mathrm{g}}} = \frac{c}{l}\tau_{\mathrm{g}} = \frac{c}{l}\cdot\frac{\partial\theta(\omega)}{\partial\omega}, \tag{11}$$

where c denotes the speed of light in vacuum, v_{g} represents the group velocity, and l is the thickness between the upper and lower electrodes. Hence, l is the sum of the thickness of

graphene and the silicon substrate. In our simulation, monolayer graphene is embedded within the Si layer, and the thickness of monolayer graphene is set to 1 nm. The thickness of monolayer graphene can be neglected compared to the thickness of the silicon substrate ($d_2 = 150$ nm). Therefore, l is approximately 150 nm in this work.

Figures 7(a)–7(e) present the group index and phase shift characteristics with graphene carrier mobility fixed at 3.5 $m^2/(V{\cdot}s)$, while the Fermi levels are set at 0.8 eV, 0.9 eV, 1.0 eV, 1.1 eV, and 1.2 eV, respectively. Strong destructive interference leads to pronounced dispersion, which significantly influences the group index, resulting in three broad and distinct peaks corresponding to the three PIT windows. Furthermore, with increasing Fermi level, the value of the transparency window $Q_{t,n}$ changes, leading to an increase in group delay $(\partial\theta(\omega)/\partial\omega)$, thereby producing a higher group index. The corresponding group indices are 1134, 1333, 1608, 1838, and 2020, respectively (black dots in Figs. 7(a)–7(e)). Because the group delay is given $\tau_g = n_g l/c$, the corresponding group delays are 0.57 ps, 0.67 ps, 0.80 ps, 0.92 ps, and 1.01 ps, respectively. It can be observed that, at constant carrier mobility, the slow-light device exhibits a gradual increase in group index as the Fermi level increases, reaching a maximum value of 2020.

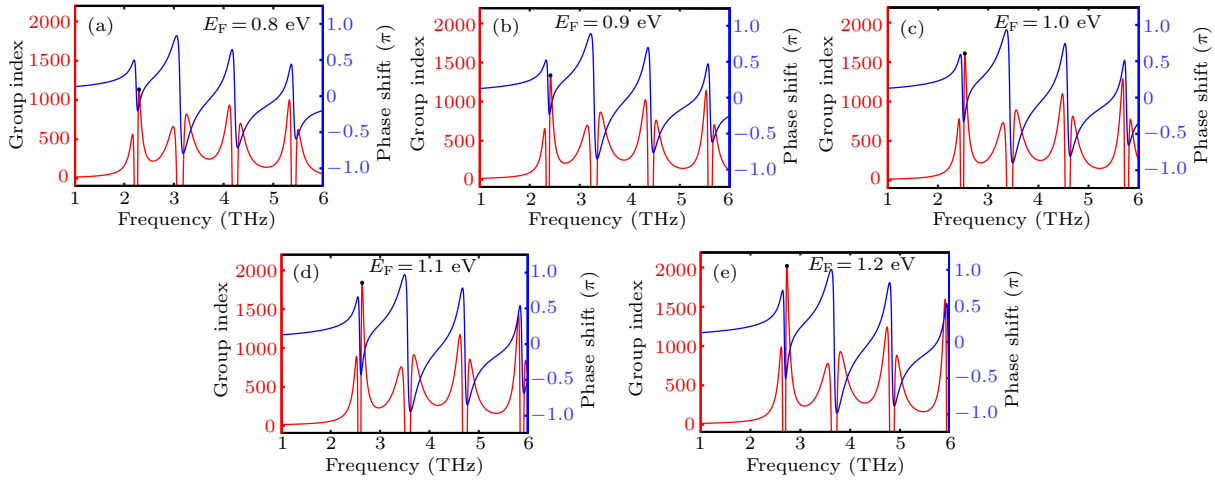


Fig. 7. (a)–(e) Group index and phase shift at Fermi levels of 0.8 eV, 0.9 eV, 1.0 eV, 1.1 eV, and 1.2 eV, with a carrier mobility of $\mu = 3.5$ $m^2/(V{\cdot}s)$, respectively.

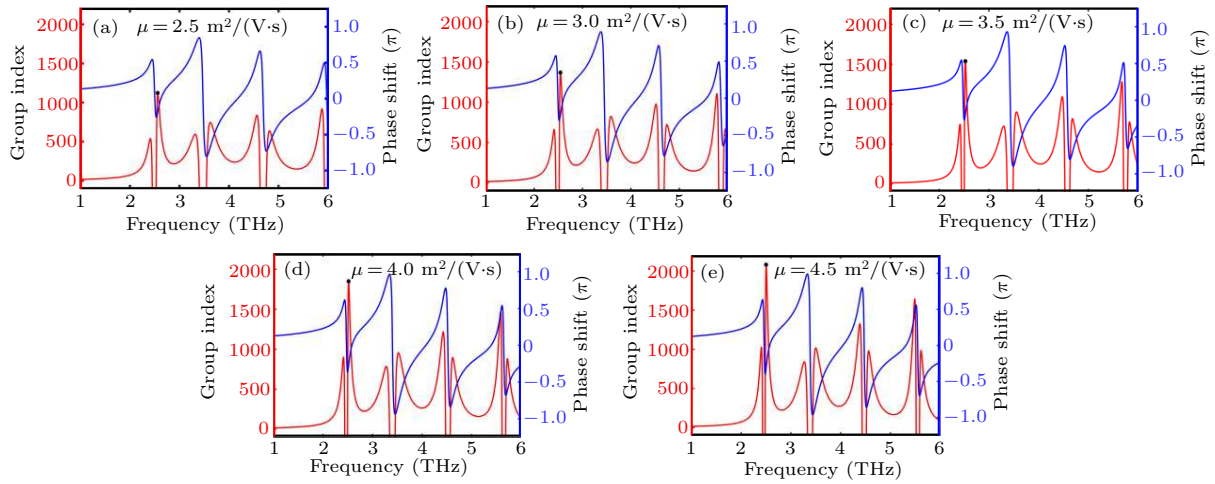


Fig. 8. (a)–(e) Changes in group index and phase shift at graphene carrier mobilities of 2.5 $m^2/(V{\cdot}s)$, 3.0 $m^2/(V{\cdot}s)$, 3.5 $m^2/(V{\cdot}s)$, 4.0 $m^2/(V{\cdot}s)$, and 4.5 $m^2/(V{\cdot}s)$ with a Fermi level of $E_F = 1.0$ eV, respectively.

Subsequently, with the Fermi level maintained constant, the group index and phase shift were examined under different carrier mobility conditions. Figures 8(a)–8(e) present the group index and phase shift characteristics at graphene carrier mobilities of 2.5 $m^2/(V{\cdot}s)$, 3.0 $m^2/(V{\cdot}s)$, 3.5 $m^2/(V{\cdot}s)$, 4.0 $m^2/(V{\cdot}s)$, and 4.5 $m^2/(V{\cdot}s)$, respectively. Significant phase shifts are observed, and strong destructive interference leads to pronounced dispersion. This dispersion directly influences the group index, resulting in three broad and distinct peaks associated with the three PIT windows. Additionally, with the Fermi level fixed at 1.0 eV, $Q_{t,n}$ varies with increasing mobility, leading to a change in group delay $(\partial\theta(\omega)/\partial\omega)$, and consequently an increase in the group index. Notably, the corresponding group indices are 1123, 1367, 1537, 1851, and 2079, respectively, as indicated by the black dots in Figs. 8(a)–8(e). The corresponding group delays are 0.56 ps, 0.68 ps, 0.77 ps,

0.93 ps, and 1.04 ps, respectively. At a given Fermi level, the group index of the slow-light device also increases gradually with carrier mobility, reaching a maximum value of 2079. Moreover, the prepared patterned graphene planar metasurface demonstrates superior slow-light performance compared with previous devices. This investigation provides insight into slow-light dynamics in graphene and indicates potential applications in high-sensitivity sensors, high-performance slow-light devices, optical modulators, and dynamically tunable optical filters.[44]

Based on the above analysis, at a Fermi level of 1.0 eV and a carrier mobility of 4.5 $m^2/(V{\cdot}s)$, the group index reaches 2079. This result demonstrates that the device exhibits excellent slow-light performance. Moreover, this value is significantly higher than that obtained by adjusting the graphene Fermi level alone. This comparison indicates that, relative to Fermi level tuning, regulating carrier mobility can more effectively enhance the slow-light effect. To further assess the slow-light performance of the proposed structure, a series of comparative analyses was conducted. As summarized in Table 1, the designed structure exhibits superior slow-light capability, achieving a group index as high as 2079 in the terahertz frequency range. Therefore, these results demonstrate that the performance of the proposed metasurface is obviously better than those of the previously reported slow-light devices. The proposed structures and results may provide strong guidance towards dynamically tunable and excellent slow-light and light-storage devices.

Recently, in some terahertz metasurfaces, high experimental Q factors have been achieved by utilizing bound state in the continuum (BIC) resonance.[45,46] Slow-light effect with a measured high group delay has also been obtained.[47,48] The high Q factor and outstanding slow-light effect in the metasurface also show exciting prospects in realizing high-performance slow light and light storage devices for promoting terahertz applications.[49,50]

Table 1. Maximum group indices with graphene-based PIT systems.

Reference/year	Structure model	PIT configuration	Maximum group index
[51]/2022	Single-layer patterned graphene	Dual-PIT	542
[40]/2023	Single-layer graphene block and strips	Single-PIT	430
[52]/2023	Single-layer patterned graphene	Single-PIT	658
[53]/2023	Single-layer graphene block and strips	Quintuple-PIT	604
[54]/2023	Single-layer graphene blocks and strips	Triple-PIT	1036
[42]/2024	Single-layer E-type graphene	Triple-PIT	1021
[55]/2024	Single-layer 4L-shaped graphene	Single-PIT	980
[56]/2025	Single-layer patterned graphene	Single-PIT	562
[57]/2025	Single-layer patterned graphene	Dual-PIT	870
[58]/2026	Triple-layer patterned graphene	Dual-PIT	481
Our work	Single-layer patterned graphene	Triple-PIT	2079

3.4. Tuning of structural parameters

To evaluate the tolerance of the device to design and fabrication deviations, two key structural parameters, H_3 and L_5, are selected for analysis. H_3, with a value of only 0.2 μm, represents the smallest feature in the structure, making it a critical parameter for assessing fabrication robustness. L_5 is selected because it directly determines the resonant behavior of the independent bright mode G2. Together, these parameters provide a comprehensive evaluation of fabrication tolerance. Figures 9 and 10 illustrate the influence of H_3 and L_5 on device performance, respectively.

As shown in Figs. 9(a1)–9(c1), when H_3 varies from its default value of 0.2 μm to 0.1 μm or 0.3 μm, the four transmission dips exhibit only minor frequency shifts. For $H_3 =$ 0.1 μm, dip 1 shifts downward by 0.18 THz, dip 2 shifts upward by 0.07 THz, dip 3 shifts upward by 0.22 THz, and dip 4 shifts downward by 0.09 THz relative to the reference case ($H_3 = 0.2$ μm). For $H_3 = 0.3$ μm, dip 1 remains unchanged, dip 2 shifts downward by 0.08 THz, dip 3 shifts downward by 0.18 THz, and dip 4 shifts downward by 0.05 THz. The maximum frequency shift among all dips is 0.22 THz, while the overall line shape remains well preserved. Thus, despite

these parameter variations, the transmission spectrum of the device remains highly stable, with negligible changes in both line shape and resonance frequency.

Moreover, Figs. 9(a2)–9(c2) show the group index as H_3 varies. At $H_3 = 0.1$ μm, the group index is 1879. When H_3 increases to 0.3 μm, the group index is 1929. This reduction corresponds to a modest decrease relative to the optimal value. Notably, even under these variations, the group index does not significantly degrade from its maximum value, indicating that the device maintains high slow-light performance despite structural deviations.

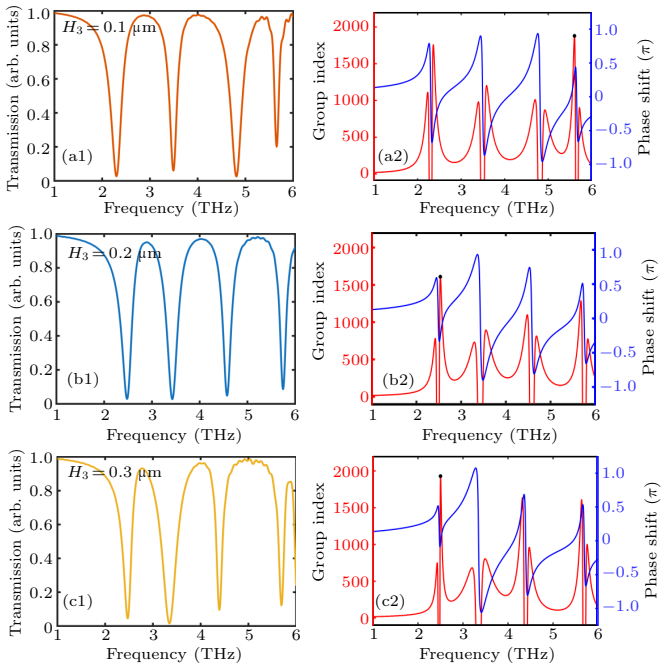


Fig. 9. (a1)–(c1) The corresponding variations of the triple-PIT curves as the parameter H_3 is tuned from 0.1 μm to 0.3 μm (the default length of H_3 is 0.2 μm). (a2)–(c2) The corresponding changes in group index and phase shift with the varying parameter H_3 in 0.1–0.3 μm.

Similarly, the transmission spectrum remains largely unaffected, as shown in Figs. 10(a1)–10(c1). When L_5 deviates from its default value of 1.4 μm to 1.2 μm or 1.6 μm, the overall spectral response is preserved. Taking the reference case ($L_5 = 1.4$ μm) as a benchmark, the frequency shifts of the four dips are as follows. For $L_5 = 1.2$ μm, dip 2 shifts downward by 0.15 THz and dip 3 shifts downward by 0.11 THz, while dip 1 and dip 4 remain unchanged. For $L_5 = 1.6$ μm, dip 1 shifts upward by 0.01 THz, dip 2 shifts upward by 0.14 THz, and dip 3 shifts upward by 0.15 THz, with dip 4 again unchanged. The maximum shift observed is only 0.15 THz, and the overall line shape remains well preserved. Thus, the device exhibits excellent spectral stability under L_5 variations, with negligible changes in both line shape and resonance frequency.

Furthermore, Figs. 10(a2)–10(c2) show how the group index varies with L_5. When L_5 is 1.2 μm, the group index is 2037. When L_5 is 1.6 μm, the group index is 1974. These results indicate that the L_5 component maintains stable performance under fabrication deviations, with a maximum reduction of 105 from the optimal value of 2079. Despite this variation, the group index remains largely stable, showing only a slight decrease relative to its optimal value. These findings confirm that the structure can effectively tolerate minor deviations that may arise during the design and fabrication processes. Such tolerance to design and fabrication variations is particularly valuable in practical applications, especially in scenarios requiring sustained high precision. This feature offers significant advantages.

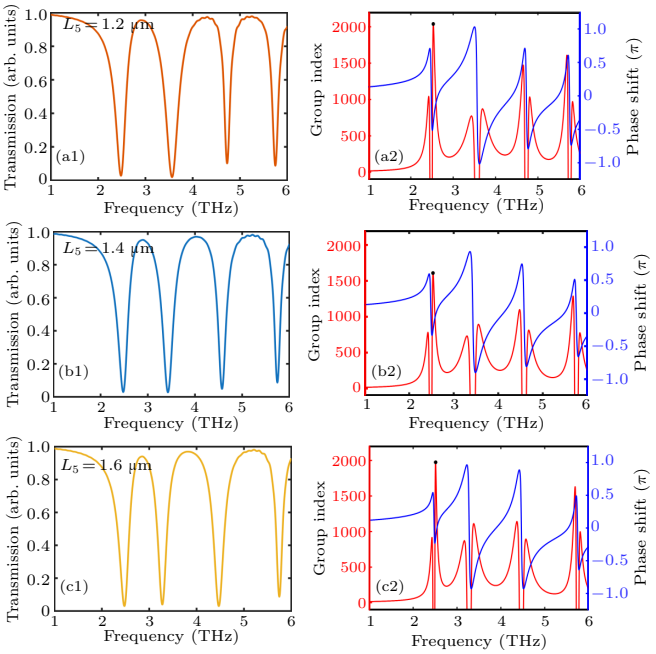


Fig. 10. (a1)–(c1) The corresponding variations of the triple-PIT curves as the parameter L_5 is tuned from 1.2 μm to 1.6 μm (the default length of L_5 is 1.4 μm). (a2)–(c2) The corresponding variations of the group index and phase shift with the varying parameter L_5 in 1.2–1.6 μm.

4. Conclusion

In conclusion, this work demonstrates a metasurface composed of monolayer graphene elements that achieves a pronounced triple-PIT effect. The theoretical framework based on CMT shows a high level of agreement with FDTD simulations. Benefiting from the electrical tunability of graphene, the Fermi level and carrier mobility can be dynamically adjusted under an applied bias voltage. Specifically, the group index of the designed triple-PIT system varies from 1134 to 2020 with increasing Fermi level of graphene at 0.8–1.2 eV. Conversely, the group index changes from 1123 to 2079 with increasing carrier mobility of graphene at 2.5–4.5 $m^2/(V{\cdot}s)$. Notably, at a Fermi level of 1.0 eV and a carrier mobility of 4.5 $m^2/(V{\cdot}s)$, a maximum group index of 2079 is achieved, which significantly exceeds that of conventional terahertz slow-light structures. Furthermore, the device exhibits excellent tolerance to design and fabrication variations. Consequently, the proposed structure provides a promising approach for the development

of terahertz slow-light devices, such as optical buffers, high-sensitivity sensors, optical switches, optical modulators, and dynamically tunable optical filters.

Acknowledgements

This project is supported by the National Natural Science Foundation of China (Grant No. 11647122), the Natural Science Foundation of Hubei Province, China (Grant No. 2022CFB475), and the Project of the Hubei Provincial Department of Education, China (Grant Nos. B2021215 and T201617).

References

[1] Zhu Z B, Li Y F, Wang J F, Qin Z, Jiang L X, Chen Y and Qu S B 2025 *Opto-Electronic Science* **4** 240026
[2] Pendry J B 2000 *Phys. Rev. Lett.* **85** 3966
[3] Pendry J, Schurig D and Smith D 2006 *Science* **312** 1780
[4] Balci S, Balci O, Kakenov N, Atar F B and Kocabas C 2016 *Opt. Lett.* **41** 1241
[5] Gao W L, Shi G, Jin Z H, Shu J, Zhang Q, Vajtai R, Ajayan P M, Kono J and Xu Q 2013 *Nano Lett.* **13** 3698
[6] Xiao T, Cheng Z and Goda K 2017 *Nanotechnology* **28** 245201
[7] Li Z, Xie M and Wang J 2023 *J. Phys. Chem. Lett.* **14** 10762
[8] Geim A K 2009 *Science* **324** 1530
[9] Novoselov K S, Geim A K, Morozov S V, Jiang D, Zhang Y, Dubonos S V, Grigorieva I V and Firsov A A 2004 *Science* **306** 666
[10] Chen J, Badioli M, Alonso-González P, Thongrattanasiri S, Huth F, Osmond J, Spasenovi M, Centeno A, Pesquera A and Godignon P 2012 *Nature* **487** 77
[11] Grigorenko A N, Polini M and Novoselov K S 2012 *Nat. Photon.* **6** 749
[12] Zayats A V, Smolyaninov I I and Maradudin A A 2005 *Phys. Rep.* **408** 131
[13] Barnes W L, Dereux A and Ebbesen T W 2003 *Nature* **424** 824
[14] Boller K J, Imamoğlu A and Harris S E 1991 *Phys. Rev. Lett.* **66** 2593
[15] Harris S E 1997 *Physics Today* **50** 36
[16] Li M, Xu H J, Xu H, Xiong C X, Zhao M Z, Liu C, Ruan B X, Zhang B H and Wu K 2020 *New J. Phys.* **22** 103030
[17] Lei P L, Nie G Z, Li H L, Li Z L, Peng L, Tang X F and Gao E D 2024 *Phys. Scr.* **99** 075512
[18] Zhao X, Yuan C, Zhu L and Yao J Q 2016 *Nanoscale* **8** 15273
[19] Xu H, Zhao M, Zheng M, Xiong C, Zhang B, Peng Y and Li H 2019 *J. Phys. D: Appl. Phys.* **52** 025104
[20] Gao E D, Liu Z, Li H, Xu H and Zhou F 2019 *Opt. Express* **27** 13884
[21] Xu H, Wang X, Chen Z, Li X, He L, Dong Y, Nie G and He Z 2021 *New J. Phys.* **23** 123025
[22] Sun G, Wang Y, Li Y, Cui Z and Chen W 2024 *Phys. Rev. B* **109** 035406
[23] Wang K R, Sun K L, Du J, Dai P J, Zhou H, Huang L J, Han Z H and Wang W 2026 *Opto-Electronic Adv.* **9** 250296
[24] Rosas S, Adi W, Beisenova A, Biswas S K, Kuruoglu F, Mei H, Kats M A, Czaplewski D A, Kivshar Y S and Yesilkoy F 2025 *Optica* **12** 178
[25] Sun G, Wang Y, Cui Z, Xie R and Zhao X 2024 *Appl. Phys. Lett.* **124** 111704
[26] Zheng L, Cheng X, Cao D, Wang G and Shen D 2014 *ACS Appl. Mater. Interfaces* **6** 7014
[27] Zheng L, Cheng X, Cao D, Wang Z, Xu D, Chao X, Shen L and Yu Y 2014 *Mater. Lett.* **137** 200
[28] Jin R and Huang L 2023 *Nano Lett.* **23** 9105
[29] Gao E, Cao G, Deng Y, Li H, Chen X and Li G 2024 *Opt. Laser Technol.* **168** 109840
[30] Liu Z, Zhang X, Zhou F, Luo X and Yi Z 2021 *Opt. Express* **29** 13949
[31] Zhang J, Zhu Z, Liu W, Yuan X and Qin S Q 2015 *Nanoscale* **7** 13530
[32] Wu D, Wang M, Feng H, Xu Z X and Liu Y P 2019 *Carbon* **155** 618
[33] Falkovsky L A and Varlamov A A 2007 *Eur. Phys. J. B* **56** 281
[34] Liang H, Ruan S, Zhang M, Su H and Li I L 2015 *Appl. Phys. Lett.* **107** 824
[35] Zhang X, Zhou F Q, Liu Z M, Zhang Z B, Qin Y P, Zhuo S S, Luo X, Gao E D and Li H J 2021 *Opt. Express* **29** 29387
[36] Skulason H S, Nguyen H V, Guermoune A, Sridharan V, Siaj M, Caloz C and Szkopek T 2011 *Appl. Phys. Lett.* **99** 153504
[37] Qin C, Wang B, Huang H, Long H and Lu P 2014 *Opt. Express* **22** 25324
[38] Wang Z, Han N M, Wu Y, Xu L and Kim J K 2017 *Carbon* **123** 385
[39] Fei Z, Rodin A S, Andreev G O, Bao W, McLeod A S, Wagner M, Zhang L M, Zhao Z, Thiemens M and Dominguez G 2012 *Nature* **487** 82
[40] Li M, Xu H, Yang X, Xu H, Liu P, He L, Nie G, Dong Y and Chen Z 2023 *Results Phys.* **52** 106798
[41] Cheng H, Chen S, Yu P and Duan X 2013 *Appl. Phys. Lett.* **103** 203112
[42] Lei P L, Nie G Z, Li H L, Liu N L, Li Z L, Liang P, Tang X F and Gao E D 2024 *Opt. Express* **32** 25435
[43] Lu Q, Wang Z Z, Huang Q Z, Jiang W, Wu Z J and Wang Y 2017 *J. Lightwave Technol.* **35** 1710
[44] Yi H, Zhou M, Gao E, Xiang Q Q, Yang H, He H R, Zhu Z Y, Liu S B, Yu T, Pan M, Guo R, Lu G B, Deng Y and Cao G T 2026 *Opt. Lett.* **51** 1883
[45] Shi W, Gu J, Zhang X, Xu Q, Han J, Yang Q, Cong L and Zhang W 2022 *Photon. Res.* **10** 810
[46] Sun G, Wang Y, Xie R, Chen X, Li Y, Chen W, Fan K, Cui Z and Zhao X 2025 *Appl. Phys. Rev.* **12** 011422
[47] Wang Y, Sun G, Chen W, Zhang X, Li Y, Fan K, Cui Z, You Z and Zhao X 2025 *Phys. Rev. Appl.* **24** 014039
[48] Rozman N, Fan K and Padilla W J 2024 *ACS Photon.* **11** 1893
[49] Zhang Y, Zhang L, Jiang M, Xi C, Hu F, Zhou Y, Lin S, Xu X and Zhao Z 2025 *Chin. Phys. Lett.* **42** 100405
[50] Zhang Y, Li C, Luan J, Zhao M, Gao D and Li P 2024 *Chin. Phys. B* **33** 104210
[51] Tang B, Guo Z and Jin G 2022 *Opt. Express* **30** 35554
[52] Wang X Y, Chen C, Gao P, Dai Y W, Zhao J M and Lu X Y 2023 *IEEE J. Sens.* **23** 4794
[53] Cheng J, Liu Z M, Zhou F Q, Luo X, Yang G X, Xie Y D and Yang R H 2023 *J. Phys. D: Appl. Phys.* **56** 405102
[54] Zhou X, Xu Y, Li Y, Cheng S, Yi Z, Xiao G, Wang Z and Chen Z 2023 *Commun. Theor. Phys.* **75** 120
[55] Tao L Y, Deng X H and Zhang P S 2024 *Opt. Express* **32** 2097
[56] Li H, Li X, Wu Y and Gao E 2025 *J. Opt. Soc. Am. B* **42** 145
[57] Li J S, Zhai Y X and Guo F L 2025 *Opt. Commun.* **581** 131607
[58] Xu Z R, Wang X J, Chen Z Q, Nie G Z and Xu H 2026 *J. Opt. Soc. Am. B* **43** 262